Bistatic Radar Imaging of the Marine Environment-Part I: Theoretical Background

A. Arnold-Bos, A. Khenchaf, A. Martin

Bistatic radar imaging of the marine environment. Part I: theoretical background

Andreas Arnold-Bos, *Student Member, IEEE*, Ali Khenchaf, *Member, IEEE*, Arnaud Martin, *Member, IEEE*

Laboratoire E^3I^2 (EA 3876)
ENSIETA (École Nationale Supérieure des Ingénieurs des Études et Techniques de l'Armement)
29806 Brest CEDEX 09, France
{arnoldan, khenchal, martinar}@ensieta.fr

***Abstract*— We describe in detail the theoretical and practical implementation aspects of a simulation for marine radars which can, in particular, be used in multistatic configurations. Since the simulator is intended to deliver pseudo-raw signals, it can be used later as a tool to benchmark and improve post-processing algorithms such as bistatic synthetic aperture radar focusing algorithms and ship wake detection algorithms. The work is divided into two parts. This paper reviews and recalls theoretical prerequisites necessary for implementing such a simulator. Included are the full derivation of the bistatic radar equation from the transmitter to the receiver, accounting also for the transmit-receive time, a description of the sea state phenomenology, a review of the theory of electromagnetic scattering from the sea surface and the presentation and validation of the method used in the simulation. A companion paper discusses the practical implementation aspects of the simulator as well as an analysis of our results.**

***Index Terms*— Marine surveillance systems, bistatic radar, bistatic scattering, radar simulation, SAR imagery.**

I. Introduction

A. Context

Despite the sheer amount of work done to improve the use of radar in the marine environment, there are still many delicate points to solve, notably when it comes to the influence and the characterization of the sea clutter as compared to the actual signature of the targets.

Current design trends for next-generation surveillance systems involve the use of multiple sensors to augment the volume of information and increase the robustness of systems to noise. When many radars look at the same scene, they can work independently and provide symbolic data that will be merged afterwards to build a synthetic view of the scene. However, the radars could also work together using a multistatic configuration, where a single transmitter would light the scene and the other sensors would act as receivers. The purported advantages of multistatic configurations as opposed to the traditional monostatic configuration – where the transmitter and the receiver are identical – are threefold: *i*) the receivers are passive thus totally stealthy, *ii*) transmitters of opportunity may be used and *iii*) some bistatic configurations might increase the visibility of ship wakes or of the ship themselves.

On the other hand, multistatic configurations are also more delicate to put into use. They involve more hardware means and require the transmitter and the receiver to be synchronized, although this tends to be easier to do today thanks to precise GPS-provided time bases. This accounts for both the lack of extensive experimental data in the literature as well as the lack of knowledge to interpret them. Perhaps because of these reasons, it seems that a significant part of the community remains skeptical about bistatic configurations.

B. Problem statement and approach

The ultimate goal of this paper and its companion "Bistatic radar imaging of the marine environment. Part II: simulation and results analysis" [1], is to describe how a radar simulator can be written by taking into account the most important constraints of the general bistatic case. In an early prototyping stage, such a simulation would help to understand what kind of configuration would be most suited to image the environment. Even when an operational system is available, a simulator remains indispensable because it enables engineers to keep a total control over the parameters of the imaging process. This is often necessary when developing post-processing tools and investigating new target detection and tracking strategies. Radar simulators are common place in the monostatic case, see *e.g.* [2]–[6]. Yet, no such work has been done in the bistatic case to the best of our knowledge. Since we furthermore consider the marine environment, this adds additional constraints on the simulation. Note that the topic of this work really is the design and the validation of the simulation strategy but not the exploitation of the simulator to find an "optimal" configuration (the notion of optimality requires application-dependent criteria and metrics): this is left for future work.

This paper, besides this introduction, aims at recalling the theoretical background necessary to understand the radar imaging process and to build a simulation, and clarifying things that are sometimes taken as granted in the literature with a thorough treatment. First, the free space propagation process is described in section II. The bistatic and polarimetric radar equation is derived (section II-A) with a careful treatment of the various polarimetric frame changes. Subsection II-B presents the derivation of the transmission delay in the

This work was supported by a grant awarded by the Regional Council of Brittany.

bistatic case. Section III presents the spectral description of the sea surface. Then, the important aspect of the radar cross section (RCS) modeling is tackled, bearing in mind that the method should be a good compromise between speed and accuracy. Accordingly, the paper ends with the presentation and the validation of a semi-deterministic, semi-statistical RCS computation method suitable for the simulation of a discretized ocean surface in any bistatic configuration. It should be noted that even if the marine environment is considered here, most of the notions are also valid for ground imaging radar.

C. Notations and conventions

All frames are orthonormal and direct. Boldface indicates a vector or a matrix ($\mathbf{V}$); the circumflex accent denotes an unitary vector ($\hat{\mathbf{u}}$). Variables written without boldface are scalars. When a vector variable is written without boldface, then its scalar norm is used. Finally, $\{\mathbf{v}\}_{\mathcal{F}}$ means that we consider the coordinates of vector $\mathbf{v}$ in frame $\mathcal{F}$.

II. Elementary contribution of a facet

A. The bistatic and polarimetric radar equation

To obtain the contribution of a single facet, the whole radar chain must be considered. This begins at the transmitting antenna. We consider here the case of aperture antennas, since, after a few simplifying assumptions stated below, the analytical solution in the polarimetric case is easy to compute. Today, slotted arrays or patch antennas are commonly used too, but their analytical modeling is more difficult; besides, the physical phenomena are more easily felt with simple aperture. If an experimental solution is not available, it is customary to approximate antennas by perfect apertures. The notations of figure 1 are used.

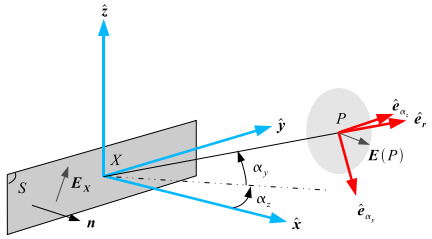

Fig. 1. Notations used to define the transmitted electric field.

A feeder illuminates the antenna, thus creating an electric field on its surface. As a first approximation, the direction of the electric field on the surface is constant. As a result, the field $\mathbf{E_X}$ at a point P' of the surface can be written as:

$$\mathbf{E_X}(P',t) = E_0 s_X(t) I(P') \hat{\mathbf{p}} \tag{1}$$

where I is the illumination pattern of the feeder, s_X is the transmitted signal and $\hat{\mathbf{p}}$ is the so-called polarization vector of the antenna. The polarization vector has components $(0, p_y, p_z)$ in the transmitter's frame $\mathcal{X}(\hat{\mathbf{x}}, \hat{\mathbf{y}}, \hat{\mathbf{z}})$. Signal s_X is another parameter of the simulator; in the rest of the paper, it is taken as a rising frequency ramp of bandwidth B centered around a carrier f_0 and of duration T_c.

To compute the field radiated at a given point P in space, we assume the antennas to be perfect conductors and that the Fraunhoffer approximation holds. The radiated field can then be written as [7]:

$$\mathbf{E}(P,t) = jk_e \frac{e^{-jk_e r}}{2\pi r} (\hat{\mathbf{n}} \times \mathbf{D}(P,t)) \times \hat{\mathbf{e}}_r \tag{2}$$

with:

$$\mathbf{D}(P,t) = \iint_{P' \in S} \mathbf{E_X}(\mathbf{XP}', t) e^{-jk_e . \mathbf{XP}.\mathbf{XP}'} \mathrm{d}S(P') \tag{3}$$

where X is the origin of the aperture, $\hat{\mathbf{n}}$ is the local normal to the aperture, $r = ||\mathbf{XP}||$ and k_e is the electromagnetic wavenumber. Since the field $\mathbf{E_X}$ has a constant direction, this simplification can be made:

$$\mathbf{D}(P,t) = E_X(t) g(\alpha_y, \alpha_z) \hat{\mathbf{p}} \tag{4}$$

The antenna pattern g yields the amplitude of the electric field diffracted by the aperture in the direction given by angles α_y and α_z. Equation 2 thus becomes:

$$\mathbf{E}(P,t) = jk_e \frac{e^{-jk_e r}}{2\pi r} E_X(t) g(\alpha_y, \alpha_z) (\hat{\mathbf{n}} \times \hat{\mathbf{p}}) \times \hat{\mathbf{e}}_r \tag{5}$$

We write $\hat{\mathbf{E}} = (\hat{\mathbf{n}} \times \hat{\mathbf{p}}) \times \hat{\mathbf{e}}_r$; since we are in the far field, $\hat{\mathbf{E}}$ lives in a plane. In the wave's frame $\mathcal{W}(\hat{\mathbf{e}}_{\alpha_y}, \hat{\mathbf{e}}_{\alpha_z}, \hat{\mathbf{e}}_r)$, $\hat{\mathbf{E}}$ is entirely defined by the two components $\hat{E}_{\alpha_y}$ and $\hat{E}_{\alpha_z}$ while the third component is always zero:

$$\begin{bmatrix} \hat{E}_{\alpha_y} \\ \hat{E}_{\alpha_z} \end{bmatrix}_{\mathcal{W}} = \underbrace{\begin{bmatrix} -\cos\alpha_z & 0 \\ \sin\alpha_y . \sin\alpha_z & \cos\alpha_y \end{bmatrix}}_{\mathbf{A}} \begin{bmatrix} p_z \\ p_y \end{bmatrix}_{\mathcal{X}} \tag{6}$$

Matrix $\mathbf{G_X} = g(\alpha_y, \alpha_z)\mathbf{A}$ allows to write the polarization of the transmitted wave as well as the directivity of the antenna as a function of the transmitter's polarization vector. Matrix $\mathbf{G_X}$ is either computed analytically for simple antennas (rectangular, elliptic), or acquired experimentally for real antennas.

Thanks to expression (6), the local incident electric field over the surface of a target is known. Now that this is acquired, the field $\mathbf{E}'(P,t)$ reflected by the target must be computed. The frame conventions given in figure 2 show how, given the incident wave's frame $\mathcal{I}(\hat{\mathbf{e}}_v, \hat{\mathbf{e}}_h, \hat{\mathbf{e}}_r)$ and the scattered wave's frame $\mathcal{S}(\hat{\mathbf{e}}_{v'}, \hat{\mathbf{e}}_{h'}, \hat{\mathbf{e}}_{r'})$, the attenuation and depolarization of the scattered wave can be described by a (complex) scattering matrix $\mathbf{S} = [S_{mn}]$:

$$\begin{bmatrix} E'_v(P,t) \\ E'_h(P,t) \end{bmatrix}_{\mathcal{S}} = \underbrace{\begin{bmatrix} S_{vv} & S_{hv} \\ S_{vh} & S_{hh} \end{bmatrix}}_{\mathbf{S}} \begin{bmatrix} E_v(P,t) \\ E_h(P,t) \end{bmatrix}_{\mathcal{I}} \tag{7}$$

The expression of $\mathbf{S}$ depends on the surface. It will be discussed later in the case where a rough surface is considered, in particular the ocean. It is important to notice that, when computing $\mathbf{E}'(P)$ from $\mathbf{E}(P)$, the incident wave is described by its two components in the incident wave's frame $\mathcal{I}$ and not in $\mathcal{W}$ which was used earlier to get the field created by the transmitter. Here, $\hat{\mathbf{e}}_v$ is in the plane of incidence, *i.e.* $\hat{\mathbf{e}}_h = \hat{\mathbf{e}}_r \times \hat{\mathbf{z}}_l$ where $\hat{\mathbf{z}}_l$ is the local normal to the surface of

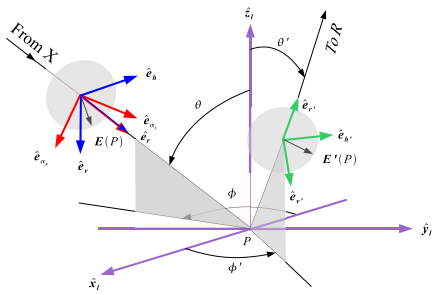

Fig. 2. Notations used to define the bistatic scattering in a local facet's frame. Vectors $\hat{\mathbf{e}}_v$ and $\hat{\mathbf{e}}_{v'}$ are in the same plane as the local normal $\hat{\mathbf{z}}_l$.

the target. The electric field in $\mathcal{I}$ is merely deduced from the electric field in $\mathcal{W}$ by a rotation $\mathbf{R_1}$:

$$\begin{bmatrix} E_v(P,t) \\ E_h(P,t) \end{bmatrix}_{\mathcal{I}} = \underbrace{\begin{bmatrix} \hat{\mathbf{e}}_{\alpha_y}.\hat{\mathbf{e}}_v & \hat{\mathbf{e}}_{\alpha_y}.\hat{\mathbf{e}}_h \\ \hat{\mathbf{e}}_{\alpha_z}.\hat{\mathbf{e}}_v & \hat{\mathbf{e}}_{\alpha_z}.\hat{\mathbf{e}}_h \end{bmatrix}}_{\mathbf{R_1}} \begin{bmatrix} E_v(P,t) \\ E_h(P,t) \end{bmatrix}_{\mathcal{W}} \quad (8)$$

Once the reflected wave at the vicinity of the target is known, the field at the center of the receiving antenna can be computed as well. First, the field must be expressed in the received wave's frame $\mathcal{W}'(\hat{\mathbf{e}}_{\alpha'_y}, \hat{\mathbf{e}}_{\alpha'_z}, -\hat{\mathbf{e}}'_r)$, as described in figure 3. The transformation from frame $\mathcal{S}$ to frame $\mathcal{W}'$ is done thanks to another rotation $\mathbf{R_2}$ followed by an axis inversion which accounts for the fact that the backscattering alignment convention is used:

$$\begin{bmatrix} E'_v(P,t) \\ E'_h(P,t) \end{bmatrix}_{\mathcal{W}} = \underbrace{\begin{bmatrix} \hat{\mathbf{e}}_{\alpha'_y}.\hat{\mathbf{e}}_{v'} & \hat{\mathbf{e}}_{\alpha'_z}.\hat{\mathbf{e}}_{v'} \\ \hat{\mathbf{e}}_{\alpha'_y}.\hat{\mathbf{e}}_{h'} & \hat{\mathbf{e}}_{\alpha'_z}.\hat{\mathbf{e}}_{h'} \end{bmatrix}}_{\mathbf{R_2}} \begin{bmatrix} E'_v(P,t) \\ E'_h(P,t) \end{bmatrix}_{\mathcal{S}} \quad (9)$$

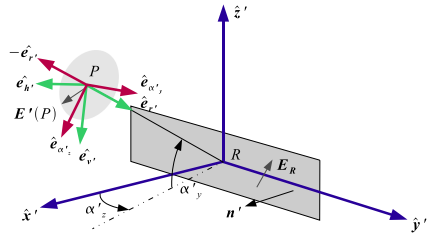

Fig. 3. Notations used to define the received electric field.

The reciprocity theorem allows to compute the electric field created by point P on the surface of the receiver, and write to it in the receiver's frame $\mathcal{R}(\hat{\mathbf{x}}', \hat{\mathbf{y}}', \hat{\mathbf{z}}')$:

$$\{\mathbf{E_R}\}_{\mathcal{R}}(t) = jk_e \frac{e^{-jk_e r'}}{2\pi r'} g'(\alpha_y, \alpha_z) \left\{\hat{\mathbf{p}}'^t\right\}_{\mathcal{R}} \mathbf{A}'^t \{\mathbf{E}'(P,t)\}_{\mathcal{W}'} \quad (10)$$

where $\hat{\mathbf{p}}'$ is the receiver's polarization vector (written in frame $\mathcal{R}$), $\mathbf{A}'$ is the equivalent to matrix $\mathbf{A}$ discussed earlier, $r' = ||\mathbf{PR}||$ and g' describes the aperture of the receiver. We write $\mathbf{G_R} = g'(\alpha_y, \alpha_z)\mathbf{A}'$.

When putting everything together, the so-called polarimetric bistatic radar equation is obtained:

$$\{\mathbf{E_R}(t)\}_{\mathcal{R}} = -k_e^2 \frac{e^{-jk_e(r+r')}}{4\pi^2 r.r'} \times \ldots \\ \{\hat{\mathbf{p}}'^t\}_{\mathcal{R}} \mathbf{G_R}^t \mathbf{R_2} \mathbf{S} \mathbf{R_1} \mathbf{G_X} \{\hat{\mathbf{p}}\}_{\mathcal{X}} E_0(t) \quad (11)$$

B. Bistatic time of flight

To complete the radar equation, the total distance $r + r'$ traveled by the electromagnetic wave must be known. This distance accounts for the free-space distance loss as well as the Doppler effect. Following Airiau and Khenchaf [7], we assume that we know the position $\mathbf{T}(t_0)$, $\mathbf{P}(t_0)$ and $\mathbf{R}(t_0)$ and the speeds (supposed to be constant) $\mathbf{V_X}$, $\mathbf{V_P}$ and $\mathbf{V_R}$ of the transmitter, the target and the receiver at time t_0. We know t_X, the time when the signal has been transmitted. The problem is to get the time t_R when the signal is received and the time of flight $\Delta t = t_R - t_X$. If t_P is the time when the signal is reflected by the target and c_0 the light velocity, then:

$$r = c_0(t_P - t_X) \quad (12)$$

$$r = ||\mathbf{P}(t_P) - \mathbf{X}(t_X)|| \\ = ||\mathbf{XP}(t_X) + \mathbf{V_P}(t_P - t_X)|| \quad (13)$$

with:

$$\mathbf{XP}(t_X) = \mathbf{XP}(t_0) + (\mathbf{V_P} - \mathbf{V_X})(t_X - t_0) \quad (14)$$

Equaling (12) and (13), squaring it, and solving for $t_P - t_X$ yields:

$$t_P - t_X = \frac{\mathbf{XP}(t_X).\mathbf{V_P} + \sqrt{\Delta_1}}{c_0^2 - V_P^2} \quad (15)$$

where

$$\Delta_1 = ||\mathbf{XP}(t_X).\mathbf{V_P}||^2 + (c_0^2 - V_P^2)||\mathbf{XP}(t_X)||^2 \quad (16)$$

Similarly:

$$r' = c_0.(t_R - t_P) \quad (17)$$

$$r' = ||\mathbf{R}(t_R) - \mathbf{P}(t_P)|| \\ = ||\mathbf{PR}(t_P) + (t_R - t_P)\mathbf{V_X}|| \quad (18)$$

which yields:

$$t_R - t_P = \frac{\mathbf{PR}(t_P).\mathbf{V_R} + \sqrt{\Delta_2}}{c_0^2 - V_R^2} \quad (19)$$

with

$$\Delta_2 = ||\mathbf{PR}(t_P).\mathbf{V_R}||^2 + (c_0^2 - V_R^2)||\mathbf{PR}(t_P)||^2 \quad (20)$$

and:

$$\mathbf{PR}(t_P) = \mathbf{PR}(t_X) + (\mathbf{V_R} - \mathbf{V_P})(t_P - t_X) \quad (21)$$

The interval of time between the arrival of two consecutive pulses varies as X, P and T move. The variation in the time of flight also compresses or dilates the pulses, causing a frequency shift (in reality, both phenomena are two aspects of the Doppler effect); indeed, depending on the configuration the end of the pulse may travel a different distance than the beginning of the pulse. If the time of flight at the beginning of the pulse is $\Delta t(t_0)$, and the time of flight at $t_0 + dt$ is

$\Delta t(t_0+dt)$, the whole pulse is squeezed or dilated in time by ratio:

$$\rho_{\text{Doppler}} \approx 1 + \left[\frac{d\Delta t}{dt}\right]_{t=t_0} \tag{22}$$

If speeds are constant, this term is constant at the first order on a whole pulse. The received signal will then be a chirp of duration $\rho_{\text{Doppler}} T_c$ centered around $f_0/\rho_{\text{Doppler}}$ and sweeping a bandwidth B/ρ_{Doppler}.

III. Physical and geometrical model of the sea surface

The scattering properties of the sea depend both on its electromagnetic characteristics and its shape. The electromagnetic characteristics are defined by the dielectric constant which in turn depends on the temperature and the salinity [8]. As for the geometric properties, sea is generally modeled as a random height field considered as a function of the position (x, y) and time t. When the wind speed is low to moderate, a first-order approximation of the sea surface can be obtained. The sea is described as a linear superposition of individual sinusoidal waves, each having a certain amplitude, pulsation, initial phase, and direction. This spectral representation is coherent with the linearized Navier-Stokes equations with the boundary conditions describing the equilibrium of the air/sea interface [9], and is valid for small surface slopes, and small waves amplitude (in front of their wavelength). The shape of the power spectral density (PSD) of the wave height function $h(x, y)$ at a fixed time t has been determined empirically during numerous oceanographic trials. The PSD is a 2D function $\mathcal{S}$, generally written as the product of two components:

$$\mathcal{S}(\mathbf{K}, ...) = \frac{1}{K}\mathcal{S}_{\text{1d}}(K, ...)\mathcal{S}_{\text{dir}}(\psi, ...) \tag{23}$$

In this equation, $\mathbf{K} = [K_x, K_y]$ is the (ocean) wave vector, K is its norm, $\mathcal{S}_{\text{1d}}$ is the (1D) omnidirectional wave height spectrum (also known as the amplitude spectrum) and $\mathcal{S}_{\text{dir}}$ is the so-called spread function. The role of the spread function is to describe the fact that waves will tend to be higher as the difference ψ between the direction of the waves and the direction of the wind becomes smaller. Many directional and omnidirectional spectra exist, since those are mostly derived from various series of experimental measures.

A. Omnidirectional wave height spectra

The models described by Philips [10], Pierson and Moskowitz [11], Fung and Lee [12], the JONSWAP [13] and more recently Elfouhaily [14] are probably among the most used omnidirectional spectra. The models depend on a varying number of parameters, the most important of which are the wind speed and wind direction. Generally, spectra consider fully-developed sea created when the wind has blown steadily over the surface for a long time ("old seas"), but the inverse wave age Ω or the fetch are used in more recent spectra (JONSWAP and Elfouhaily) so that younger seas can be taken into account as well. In our work, we make use of both the Elfouhaily spectrum and the Fung and Lee spectrum. The former has an unwieldy expression but the reader may find it in [14]. The latter is mathematically simpler, so we present it here to fix the ideas; we also make use of it in Part II to derive a few analytical results. Both spectra have a similar physical meaning. The Fung and Lee spectrum is an attempt at unifying and simplifying the Philips spectrum (valid for short, capillarity waves) and the five functions used by Pierson and Moskowitz to describe the amplitude spectrum for different intervals of the ocean wavenumber. Instead of five parts, the Fung and Lee spectrum can be written in two parts:

$$\mathcal{S}_{\text{1d, FL}} = \begin{cases} \mathcal{S}_{\text{1d, FL, gravity}}(K) & \text{if } K \leq 4 \text{ rad/m} \\ \mathcal{S}_{\text{1d, FL, capillary}}(K) & \text{if } K > 4 \text{ rad/m} \end{cases} \tag{24}$$

- $\mathcal{S}_{\text{1d, FL, gravity}}$ is a modified Pierson and Moskowitz spectrum describing the gravity waves:

$$\mathcal{S}_{\text{1d, FL, gravity}}(K) = \frac{1.4.10^{-3}}{K^3} \exp\left[-\frac{0.74 g_0^2}{K^2 U_{1950}^4}\right] \tag{25}$$

  where g_0 is the acceleration of gravity and U_{1950} is the wind speed at 1950 cm above the mean sea level (AMSL).
- $\mathcal{S}_{\text{1d, FL, capillary}}$ is a modified Philips spectrum valid for small scale, capillary waves:

$$\mathcal{S}_{\text{1d, FL, capillary}}(K) = a_0(1+3\bar{K}^2)\left[K(1+\bar{K}^2)\right]^{-(p+1)/2} \tag{26}$$

  where $a_0 = 0.875(2\pi)^{p-1} g_0^{(1-p)/2}$ and $p = 5 - \log_{10}(U_0)$. Here U_0 is the friction wind speed, that is, the wind speed at the sea level (in cm/s), which is related to the wind speed U_z at altitude z (in cm) by:

$$U_z = (U_0/0.4)\ln(z/Z_0) \text{ [cm/s]} \tag{27}$$

  with $Z_0 = 0.684/U_0 + 4.28.10^{-5}U_0^2 - 0.0443$ [cm]. Finally, $\bar{K} = K/K_m$. Constant K_m is equal to $\sqrt{g_0\rho/\tau}$ where ρ is the sea water density and τ is the surface tension; the computed value of K_m is 3.63 rad/m. This relation describes the exponential-like decay of the wind speed in the boundary layer above the sea surface, and is only strictly valid for one fixed sea/air temperature difference not mentioned in Fung and Lee's paper.

The Fung and Lee spectrum is theoretically valid only for wind speeds such that U_0 is above 12 cm/s, since the experimental measures leading to the spectrum have not been carried out for lower wind speeds. This excludes calm sea states (0 and 1). Similar restrictions exist for other spectra as well even if those are often conveniently forgotten. This, however, is not very disturbing in the sense that the wave heights as well as the sea RCS degenerate graciously when $U_0 \to 0$. Figure 4 provides a comparison between the Fung and Lee spectrum for gravity waves $\mathcal{S}_{\text{1d, FL, gravity}}$ (figure 4, left), the complete Fung and Lee spectrum (figure 4, middle), and the Elfouhaily spectrum with the inverse wave-age corresponding to a fully-developed sea so that conditions are the same as for the Fung & Lee spectrum (figure 4, right). Notice how the full Fung and Lee spectrum provides more energy for capillary waves but also how it has a faster decay as compared to the Pierson, gravity part. The Elfouhaily spectrum has the same aspect, with an even faster decay, and even more energy put into it. For all three spectra, when the wind speed augments, the spectrum becomes broader, which explains why waves become higher.

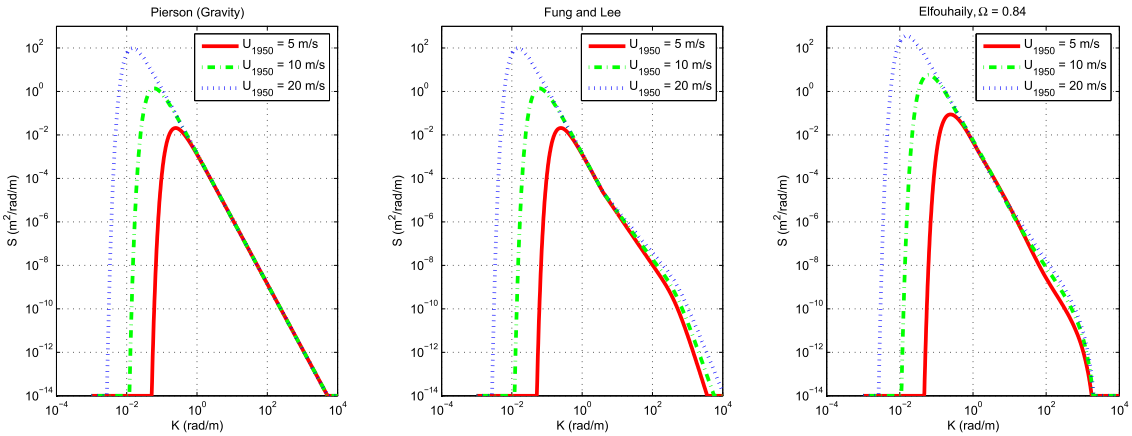

Fig. 4. Comparison between the gravity-waves Pierson-Moskowitz spectrum used as the low-frequency part of the Fung & Lee spectrum (left), the complete Fung and Lee spectrum (middle) and the Elfouhaily spectrum for the inverse wave-age corresponding to a fully-developed sea (right).

B. Directional wave height spectra

Here again, a great deal of models exist to represent the fact that the wave energy has an angular distribution as well. Longuet-Higgins [15] proposed a simple dependence to the wind direction in the form of a cosine-2s function:

$$\mathcal{S}_{\text{dir, LH}}(\mathbf{K},\psi) = \left(\frac{2^s-1}{\pi}\right)\frac{\Gamma^2(s+1)}{\Gamma(2s+1)}\cos^{2s}\left(\frac{\psi-\psi_0}{2}\right) \tag{28}$$

where $s \geq 2$ is an integer parameter, Γ is Euler's Gamma function, ψ_0 is the direction of the wind and ψ the propagation direction of the wave. In this form, the function is normalized so that its integral in the (K,ψ) space is one. However, as pointed out in the literature [12], [14], [16] the spread function should also depend on the wave number and other directional spectra have subsequently been proposed to take this into account. For instance, Fung and Lee [12] proposed:

$$\mathcal{S}_{\text{dir, FL}}(\mathbf{K},\psi) = a_1 + a_2(1-e^{-bK^2})\cos(2(\psi-\psi_0)) \tag{29}$$

with

$$a_1 = \frac{1}{2\pi} \tag{30}$$

$$a_2 = \frac{(1-\tau)/(1+\tau)}{\pi(1-\beta)} \tag{31}$$

$$\tau = \frac{0.003 + 1.92\times10^{-3}U_{1250}}{3.16\times10^{-3}U_{1250}} \tag{32}$$

with U_{1250} the wind speed at 1250 cm AMSL in m/s and β a function of the slope variance (which we took equal to zero as a first approximation).

C. Surface velocity

As mentioned in section II-B, the velocity of the target is a source of Doppler shift. The surface is assumed to be described in the orthonormal "global" frame given by vectors $\hat{\mathbf{x}}_g$, $\hat{\mathbf{y}}_g$, $\hat{\mathbf{z}}_g$, the latter being normal to the mean surface level. The velocity to be considered for the Doppler effect is the orbital velocity of a point $\mathbf{P}(x,y,z)$ of the surface. We consider here a monochromatic wave of amplitude A, of wave vector $\mathbf{K}$ and wave number ω. The orbital velocity at a $\mathbf{P}$ is then [17]:

$$\mathbf{v}(\mathbf{P}) = A\omega \times \left(\frac{\mathbf{K}}{K}\cos(\mathbf{K}.\mathbf{P}) + \hat{\mathbf{z_g}}\sin(\mathbf{K}.\mathbf{P})\right) \tag{33}$$

For small-amplitude, linear waves, this equation can be written only as a function of ω, using the dispersion relation [18], which is written here for a sea of infinite depth:

$$\omega^2 = g_0 K \tag{34}$$

The motion of facets is at the origin of several artifacts in radar images. When monostatic synthetic aperture radar (SAR) imaging is performed, waves moving along the flight track cause a slight degradation of azimuthal resolution (azimuth smearing) . Also, the azimuth location of a target in SAR images is found via the Doppler effect. If the target is not static, as is the case with waves, the image undergoes an azimuthal translation proportional to the Doppler shift. This can be the origin of a non-uniform scatterer distribution in the final SAR image which produces wave-like patterns; this phenomenon is known as velocity bunching [19]. Since the motion between two consecutive pulses as well as the speed of a facet can be simulated, this phenomenon is implicitly taken into account in the computed raw signal and is visible if SAR focusing is eventually done.

There are, however, additional non-linear hydrodynamic phenomena which affect both the surface shape as well as the velocity. They are responsible in particular, for slope asymmetry between the front and the back of gravity waves, the fact that crests are more spiky and troughs more flat. Those effects have been investigated *e.g.* by Harger [20], Gelpi and Norris [17], Toporkov [9] and Saillard *et al.* [21]. As far as velocities are concerned, a notable phenomenon is the non-linear hydrodynamic modulation of capillary waves by gravity waves; assuming a two-scales model, capillary waves at a given point are carried along gravity waves but have an additional tangent velocity due to the centripetal acceleration of the gravity wave [20]. This causes further Doppler bias, but the effect is second to the effect of linear motion [17].

IV. Deriving the scattering matrix from the sea spectra

A. Background

The scattering matrix $\mathbf{S} = [S_{pq}]$ will describe how the an incident wave, transmitted from a source at a distance r from a surface, will be reflected by said surface:

$$\{\mathbf{E}'(\mathbf{P},t)\}_{\mathcal{S}} = \mathbf{S}\frac{e^{-jk_e r}}{r}\{\mathbf{E}(\mathbf{P},t)\}_{\mathcal{I}} \tag{35}$$

When considering powers, the power scattering matrix $\mathbf{\Sigma} = [\sigma_{pq}]$ is used, where $\sigma_{pq} = S_{pq}S^{\star}_{pq}$. Since S_{pq} and σ_{pq} depend on the area of the target, the normalized scattering matrix $\mathbf{\Sigma}^0 = [\sigma^0_{pq}]$ is generally computed. Σ^0 is normalized thusly:

$$\mathbf{\Sigma}^0 = \frac{4\pi r^2}{A}\mathbf{\Sigma}$$

where A is the area of the surface. In all generality, computing the scattering matrix requires to come back to the Maxwell equations which must be solved by taking the boundary conditions on the surface into account. Methods exist to perform the integration of these equations numerically, such as the Method of Moments [22], [23], they are generally relatively precise but computationally slow and memory-intensive, thus unsuitable for large surfaces. Thus, for the kind of simulation desired here, approximate solutions must be preferred.

Two phenomena exist: specular reflection and diffuse reflection [24]. Specular reflection is caused by large-scale waves that are tilted in such a way that an electromagnetic wave will "bounce" on it according to the law of reflection. Diffuse reflection is caused by small ripples on the surface of the sea which, having more or less the same wavelength as the incoming electromagnetic wave, will interfere constructively in a certain direction: this is the well-known Bragg diffraction process. Computing the scattering matrix requires to take both phenomena into account. This can be done either by computing the contribution of each phenomena separately and then seeking to merge the contribution afterwards or by tackling the two processes simultaneously. Before describing the method we implemented, we briefly review the current state of the art concerning the computation of the scattering matrix for rough surfaces. The notations are detailed in figure 5.

B. The Kirchhoff Approximation

A common approach to tackle the specular reflection is the Kirchoff Approximation (KA) introduced by Brekjovskikh in 1952 [25], [26], described in all generality for instance in the book by Beckmann and Spizzichino [27] or Ulaby [28] and derived in the bistatic case by Barrick [29]. The method was found to give a good agreement with experimental results when close to the specular direction but quickly tends to underestimate the reflection in other directions. In the KA model, the assumption is made that the radius of curvature of the waves is large enough in front of the electromagnetic wavelength so that they may be locally approximated by a tangent plane. For high electromagnetic frequencies, the geometric optics approximation can then be used. This assumption becomes truer as the frequency increases and begins to be reasonable

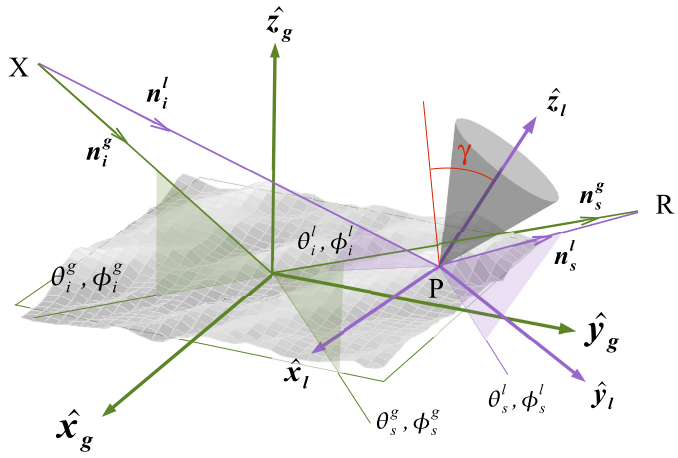

Fig. 5. Global *vs.* local frame. The global frame is relative to the mean sea level and is defined by $\mathbf{x}_g$, $\mathbf{y}_g$, $\mathbf{z}_g$, with "global" bistatic angles $(\theta_i^g, \theta_s^g, \phi_i^g, \phi_s^g)$. A local frame is defined by $\mathbf{x}_l$, $\mathbf{y}_l$, $\mathbf{z}_l$ and bistatic angles $(\theta_i, \theta_s, \phi_i, \phi_s)$. Inside the cone, reflection is specular.

above one gigahertz with respect to gravity waves (as a result, we *do not* consider lower frequencies in our work). The Kirchhoff Approximation amounts to considering that only specular points on a lighted surface will actually contribute to the received signal. In a far-field configuration, the scattering coefficients will thus be proportional to the probability of finding such specular points, given the configuration of the transmitter and the receiver:

$$\sigma_{mn} = \frac{\pi k_e^2 ||\mathbf{q}||^2}{q_z^4}|U_{mn}|^2 \mathrm{Pr}(Z_x, Z_y) \tag{36}$$

where $\mathbf{q} = k_e(\mathbf{n_s^g} - \mathbf{n_i^g}) = [q_x, q_y, q_z]$, U_{mn} is a polarimetric parameter depending on the configuration angles $(\theta_i^g, \phi_i^g, \theta_s^g, \phi_s^g)$ and on Fresnel coefficients [28]; and $\mathrm{Pr}(Z_x, Z_y)$ is the probability of finding a slope $Z_x = -q_x/q_z$ and $Z_y = -q_y/q_z$ on the sea surface. The slope probability function has been determined experimentally and fitted to an analytical curve by Cox and Munk [30]. The KA model is adequate to compute the average specular component for gravity waves, which satisfy to the large radius of curvature condition, and this for a sea of infinite area. It should be noted that the model is only valid when close to the specular direction ($\pm 20°$); when other directions are chosen, the components of $\mathbf{S}$ will be underrated since the diffuse component is not taken into account. The KA model can also be derived within the physical optics framework [28], which slightly widens the validity domain around the specular direction. Only the geometric optics solution was implemented in our work.

C. The Small Perturbations Model

The Small-Perturbations Model (SPM) is well suited to describe the diffuse component; it has first been introduced for radio waves by Rice [31] and found agreement with wave tank and outdoor experiments [32], [33] in the case of water; the method is also well-developed in the book by Ishimaru [34]. An improvement of the SPM is the Two Scales Model (TSM) proposed, for instance, by Bass and Fuks [35] and

applied to sea surfaces by Valenzuela [24] or Chan and Fung [36]. It has been recently extended both to the bistatic case and to sea applications by Khenchaf and Airiau [37].

The derivation of the Small Perturbations model begins by stating that the total electric field $\mathbf{E}$ can be written as the sum of the incident field, the reflected field (specular and diffuse) and the transmitted field. Then, a boundary condition is introduced; in the case where the surface is a perfect conductor, the condition is that the tangential field is null on the surface. The tangential field can be written as: $\mathbf{E_t} = \mathbf{E} - (\mathbf{E}.\mathbf{z}^l).\mathbf{z}^l$ where $\mathbf{z}^l$ is the local normal. Vector $\mathbf{z}^l$ is then expressed as an expansion in powers of a small quantity ϵ, like the height of the surface or its slope (in fact, both quantities have to be small). This allows to write the reflected and transmitted field as an expansion of individual electromagnetic waves in powers of ϵ. At the order zero, the reflected wave is just the specular component over a flat surface. The Small Perturbations model is usually the development to the first order of the reflected field, thus introducing some diffusion. As ϵ must be small, it is supposed that the typical sea wave height is small compared to the electromagnetic wavelength; as a result, only capillary waves are represented. It is also assumed that no multiple reflections occur. The mathematical derivation of the model allows to introduce the spectral description of the surface height, which we do know. Finally, in the bistatic case, the components of the diffusion matrix and the inter-correlation coefficients are given by:

$$\sigma_{mn} = 8k_e^4 \cos^2(\theta_i)\cos^2(\theta_s)|\alpha_{mn}|^2 \mathcal{S}(||\mathbf{K}'||, \angle(\mathbf{K}', \mathbf{u})) \tag{37}$$

where α_{mn} is a polarimetric coefficient that depends on the bistatic angles and the sea permittivity [34]; and $\mathbf{u}$ the vector defining the wind direction. $\mathbf{K}'$ is defined by:

$$\mathbf{K}' = \begin{bmatrix} k_e \sin(\theta_s)\cos(\phi_s - \phi_i) - k_e \sin(\theta_i) \\ k_e \sin(\theta_s)\sin(\phi_s - \phi_i) \end{bmatrix} \tag{38}$$

This model is shown to be suitable for the estimation of the diffuse component, but is invalid in the specular zone, where it mathematically diverges and may reach unrealistically high values in some configurations.

D. Composite models

1) The Two-Scales model (TS): This model has been introduced a long time ago (see, for instance, [24], [35]) and extended to rough surfaces and bistatic conditions more recently [37], [38]. It postulates that the ocean can be seen as the superposition of two categories of waves: gravity waves with large radius of curvature, and capillary waves, which are smaller. In reality, the transition between large waves and small waves is continuous and this is only a good-enough approximation: in fact, there is good evidence that a three-scales model could be more accurate, see for instance [39], but three-scales numerical methods would probably be slow to compute. One of the purported advantages of the TSM is to augment the angular validity domain (especially for incidence angles) of computed indexes.

The idea behind the Two-Scales model is that waves contributing to the Bragg process are locally tilted by longer waves. One then computes the scattering coefficients using the Small Perturbations model for all possible combinations of "local" bistatic angles $(\theta_i^l, \theta_s^l, \phi_i^l, \phi_s^l)$. The Two-Scales scattering coefficient is simply a weighted average of the local Small-Perturbations coefficients, the weight being proportional to the probability of occurrence of a given combination of local bistatic angles. This probability is related to the slopes probability distribution.

Interestingly enough, the few combinations of local bistatic angles which are more of a specular nature do not corrupt the weighted average, since the associated weight tends to be small: there are few specular points for a surface of infinite width. This also means that the Two-Scales model underrates specular reflection. This can be solved simply by adding the scattering coefficient obtained with the Kirchoff Approximation, to the coefficient obtained with the TSM, which is what makes it a composite model.

2) Other methods: There are other methods that try to unify the specular and the diffuse reflection in a single theory; the most recent review of those methods is probably the paper by Elfouhaily and Guérin [40]. The Small-Slope Approximation (SSA), introduced by Voronovich, is one of these; the interested reader may refer to *e.g.* [41] for the first order approximation (SSA-1) and [42] for the more precise second-order approximation (SSA-2). SSA-1 has been compared recently to the TSM in the bistatic case for sea surfaces at the ENSIETA [43]; in this paper, TSM has been shown to be close to SSA-1 but also to be more robust since SSA-1 mathematically degenerates in some very specific bistatic configurations where TSM behaves well. Besides, SSA is slower to compute than the TSM. SSA-2 probably solves the robustness issue but at an even greater computational cost. We will compare further down our own results with those obtained by Voronovitch to validate our model. The Extended Boundary Condition Method has also been proposed and implemented for rough surfaces by Franceschetti *et al.* [44], [45] and in particular for the sea by Guo and Wu [46]; this method finds agreement with the aforementioned methods and makes no assumption on scale division; it has however been used with a fractal model of sea surface which is harder to fit with physical variables such as wind speed and direction. Finally, Elfouhaily *et al.* [47] developed another composite method called the Weighted Curves Approximation but we will not discuss it in this paper.

V. Simulation of the sea scattering matrix, using a semi-deterministic two-scales model (SD-TSM)

A. Motivation

All the methods mentioned above are statistical, in the sense that the bistatic angles are given with reference to the average plane of the sea: $(\theta_i^g, \theta_s^g, \phi_i^g, \phi_s^g)$, as shown in figure 5. Once the configuration is set, a diffusion coefficient obtained for a given set of bistatic angles is an average, over an infinite sea surface, of the *real* diffusion coefficient. The average encompasses both gravity and capillary waves. The advantage is that a particular sea height map is not needed. These methods are therefore particularly suited to quickly

compute a link budget when designing a system. However, the downsides are twofold. First, even if the average is known, nothing is said about the way the RCS fluctuates around the average. The speckle noise needs to be added later. Secondly, when deterministic and/or local features such as ship wakes or oil spills are present in the image, the local RCS can be different, since the surface will sometimes be of a different nature. For these reasons, the scene a simulation must be represented as a digital elevation map, so that surface and electromagnetic properties may be changed locally for a few facets. This facet-based approach is recurrent in simulation. However, some facets may be in a specular configuration, others in a diffuse configuration. A strong emphasis is often put on the diffuse reflection process in simulation [3]–[6] which is understandable since these papers consider the case of side-looking radar with intermediate incidences where diffuse reflection contributes for most of the received power. Basically, the approach is to emulate the statistical Two-Scales method in a facet-based context. However the way they tackle the few facets in specular reflection is, in our opinion, unclear; in [5] and [6], only diffuse scattering is considered using the SPM; in [3] and [4], we understand that basically the same approach has been adopted. Yet if more diverse configurations are to be simulated, such as those that might be doable in more "exotic" bistatic configurations, locally specular reflections may have a bigger influence.

B. Description

First, a deterministic wake height map is superimposed over a particular realization of a sea height map, obtained with the sea spectrum. This procedure is described in Part II, section III-A. The resulting height map has $n \times m$ facets, each facet having a surface dS. Subpixellic structures are considered as a random, fine scale rough surface, described statistically. We obtain the scattering coefficients for each point of the surface by computing local bistatic angles with respect to local normals. The scattering coefficients are computed by assuming that the facets are, in fact, infinite, so that the KA and the SPM can be used in the local frame to get Σ_0, then the coefficient is multiplied by the area of the facet.

This resembles the Two-Scales method but for a significant difference. Here, since a small patch of sea is generated, the proportion of specular points can be important enough that the wrong, but very high values given by the SPM subroutine can significantly distort the average. SPM coefficients are sometimes of the same order than the KA: about +10 dB, sometimes many orders of magnitude higher (+90 dB), depending on the configuration. Adding the KA and TSM contributions is correct, adding the KA and SPM contribution is not.

Hence, we choose either the coefficients given by the KA if the direction is nearly specular, or the coefficients given by the SPM else. The specular region is given by an approximately $20°$ cone around the local normal. That is, when noting P a facet, and γ the angle between the bisector of angle $\hat{XPR}$ and the local normal $\hat{\mathbf{z}}_l$ to the surface at P, the reflection is specular when γ is approximately below $20°$ (see figure 5).

However, the transition between the specular and the diffuse region must be smooth. Being inspired by the approach proposed by the Applied Physics Laboratory to model underwater sound scattering [48], we decided to compute an average of the KA and TSM coefficients. The weights we came up with are:

- for co-polarizations:

$$\sigma_{nn} = (1 - w_1)\delta_{\text{SP}}\sigma_{nn,\ \text{SP}} + w_1\delta_{\text{KA}}\sigma_{nn,\ \text{K}} \tag{39}$$

- for cross-polarizations:

$$\sigma_{nm} = (1 - w_2)\delta_{\text{SP}}\sigma_{nm,\ \text{SP}} + w_2\delta_{\text{KA}}\sigma_{nm,\ \text{K}} \tag{40}$$

with:

$$\log_{10} w_1(\gamma) = -\left(\frac{\gamma}{6\pi}\right)^8 \tag{41}$$

$$\log_{10} w_2(\gamma) = -\left(\frac{\gamma}{20\pi}\right)^{1.5} \tag{42}$$

The weighting functions are polynomial in the log-space, which allows for a simple, manual tuning. The coefficients have been chosen empirically so as to somewhat minimize abrupt changes of slope at the transition between the two models, and this brings good results for all values of the bistatic angles $(\theta_i^l, \theta_s^l, \phi_i^l, \phi_s^l)$.

Figure 6 shows the value of the scattering coefficients with fixed values of θ_i^l, θ_s^l, ϕ_i^l and by letting ϕ_s vary. As stated above, it appears that the Kirchhoff approximation underrates diffuse scattering (occurring here when ϕ_s is between 20 and $160°$), compared to values given by the SPM. In turn, the latter does not behave well in the specular zone. Interpolation gives better results.

In equations (39) and (40), two factors δ_{SP} and δ_{KA} appear. Those are visibility coefficients and are equal either to zero or to one. Their meaning is as follows.

- δ_{KA} is a macroscopic visibility factor, which influences on specular reflection. For a given facet, $\delta_{\text{KA}} = 1$ if and only if the facet is visible from the transmitter and the receiver and is not hidden by another facet. The visibility is computed through a standard ray-tracing or Z-buffer procedure.
- Diffuse reflection has a local nature and the masking of one tile by another plays an irrelevant role. However, some tiles may be tilted in such a way that the ray coming from the transmitter and going to the receiver would have to cross the air/water interface, which is impossible. Only tiles such that $\hat{\mathbf{n}}_i^l.\hat{\mathbf{z}}^l < 0$ and $\hat{\mathbf{n}}_s^l.\hat{\mathbf{z}}^l > 0$ can contribute. This condition is represented by the boolean δ_{SP}, which is the local visibility factor.

The visibility factors do not play the same role everywhere. When angles θ_i^g and θ_s^g are not excessive (say below $65°$), all the waves are visible and the macroscopic visibility factor is equal to one everywhere; the ray-tracing can then be safely omitted. Conversely, when θ_i^g and θ_s^g are close to $90°$, as is the case when coastal radars are used, the macroscopic visibility factor is equal to zero everywhere; only diffuse reflection will occur and again, the ray-tracing can be omitted. In the "critical" zone going from about $65°$ to $85°$ for the angle of incidence, some tiles may be visible and others may not; in this range the ray-tracing must imperatively be used.

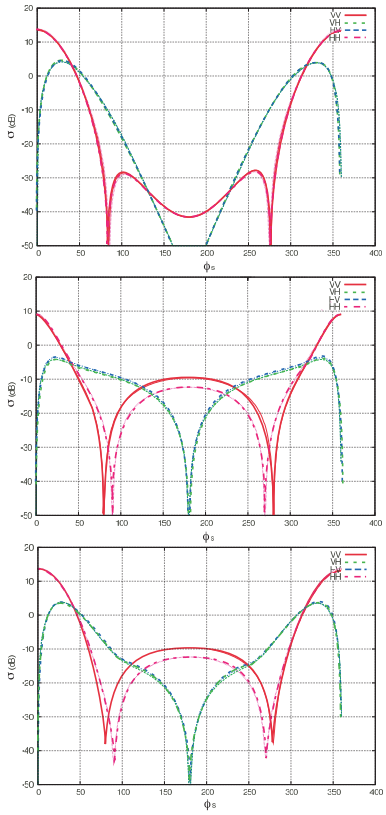

Fig. 6. Local normalized scattering coefficients, for $\theta_i^l = 20°$, $\theta_s^l = 30°$, $\phi_i^l = 0°$ and various ϕ_s^l. $U_{1950} = 4.53\, m/s$, f_0=10 GHz. Above: Kirchhoff Approximation, middle: Small Perturbations, bottom: weighted average of KA and SPM according to γ.

C. Validation

When locating the transceiver and the receiver at near infinity (here, 10^5 m) and averaging over a large surface, results similar to the conventional, statistical methods should be obtained. A surface of 512×512 tiles at a one-meter resolution has been considered here (experimentally, the average does not depend much upon the discretization step). We find an excellent agreement between our results, and those obtained by Voronovich and Zavorotni [42] using SSA-2, which they compared to experimental measures reproduced here (see figure 7). The choice of the sea spectrum can has a slight influence on the RCS, as is shown here with the Fung and Lee spectrum *vs.* the Elfouhaily spectrum. The Fung and Lee spectrum yields smaller returns than with the Elfouhaily spectrum; the explanation is that the energy in the capillary section of the spectrum tends to be lower in the Fung and Lee spectrum, as remarked previously (see figure 4). Figure 8 shows the dependency of the scattering coefficient with the wind direction, and reproduces experimental results reported by Moore and Fung [49] in the same conditions. The agreement is less evident but still well within acceptable bounds: to that respect, we quote Long [50] (chapter 6, p. 353) who reminds us that in the context: "the 'average' radar cross-section can change as much as 10 dB in a 1-minute interval". Keeping this in mind, we feel that even if there are slight differences, the actual choice of the spectrum

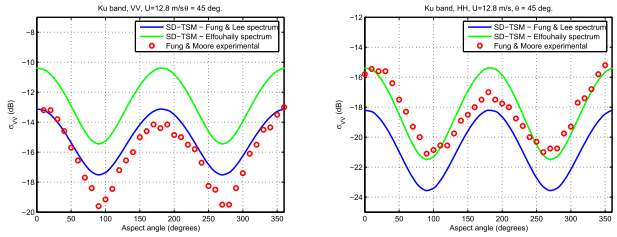

Fig. 8. Agreement test between the semi-deterministic two-scales method (SD-TSM) using the Fung and Lee spectrum [12] or the Elfouhaily spectrum [14], against experimental measures quoted after [49] at 13.9 GHz. Wind speed is at z =1950 cm.

seems not to have such a high importance as far as the RCS computation is concerned –which explains why even a crude Gaussian spectrum has been often used to model capillary waves. However, the spectrum does have a visible influence on the *texture* of the surface; the directional spectrum is the most important parameter here. Experimental measures in figure 8 show differences between the upwind and the downwind direction (0 and 180°) since actual waves tend to have steeper slopes in their direction of propagation. The linear wave superposition theory cannot model this, which explains why it predicts similar returns in both cases.

Last but not least, our method also yields quite similar results to those obtained with the Two-Scales Model and SSA-1 in the more general bistatic configurations presented in [43] but that we omitted here for the sake of brevity.

VI. Conclusion

In this paper, we recalled the theoretical background necessary to understand the bistatic imaging process in the marine environment. However, most of the equations can be re-used for the ground-imaging environment. Only the spectral representation of the surface will change to represent *e.g* hill and valleys instead of ocean waves, and the time evolution of the surface is absent, which simplifies things. Particular care was given to the different frame changes which occur during the computation of the bistatic radar equation. These frame changes are particularly important when implementing Two Scales-like methods, be it the classic, statistical method exposed in section IV-D.1, or the semi-deterministic, semi-statistical facet-based version of the TSM presented in section V and used in the simulation.

A particular note should be given for this latter version of the TSM. The idea is certainly intuitive; it was already touched upon by *e.g.* Valenzuela [24], and used in actual simulations [6]. Yet the validation of the approach has, to the best of our knowledge, not been presented satisfactorily before, especially in the bistatic case. Besides, we showed that using the SPM on a facet-per-facet basis requires a careful treatment of the transition between the specular and the diffuse zone. An approach based on a weighted average of the two components has been proposed to solve this problem.

Several aspects were however left out since they were not implemented; we mention them here for the sake of completeness. For instance, only free-space propagation was described;

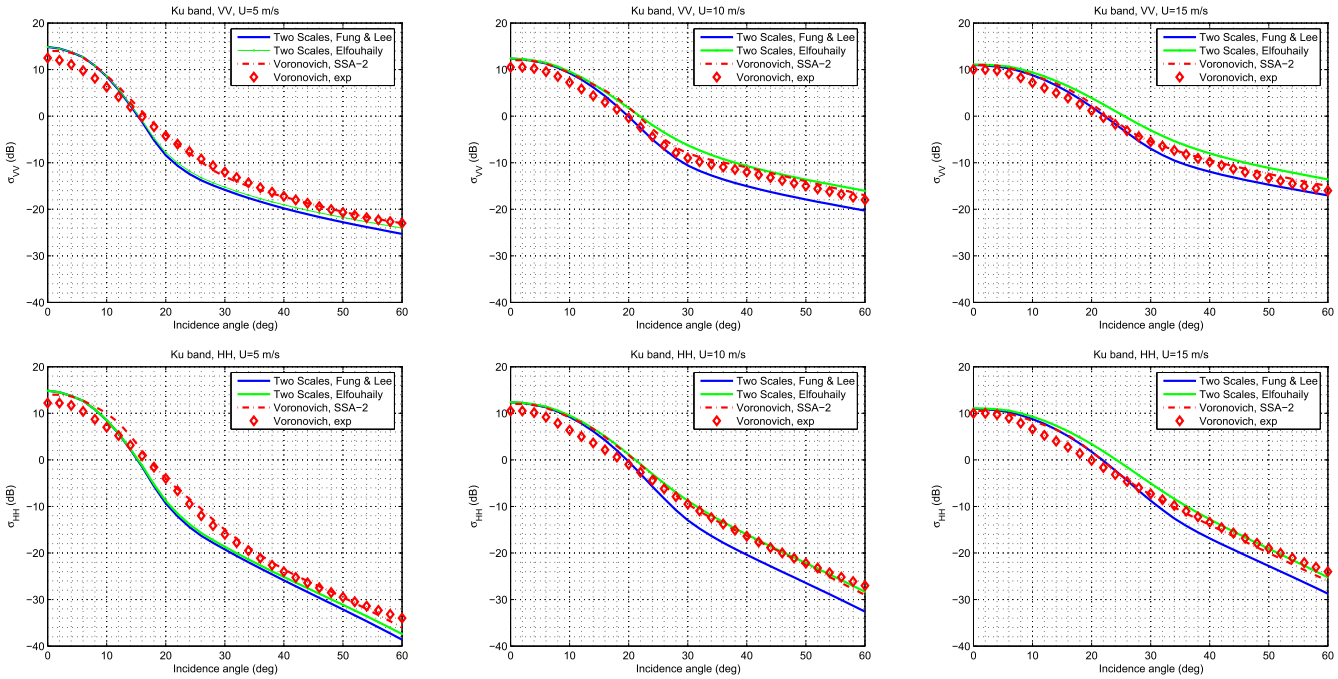

Fig. 7. Agreement test between our semi-deterministic two-scales method (Fung and Lee spectrum [12] and Elfouhaily spectrum [14]), and SSA-2 (values quoted from Voronovitch [42]), where the Elfouhaily spectrum was used. The wind speed is given $z = 10$ m AMSL and the frequency is 14 GHz.

additional propagation phenomena such as atmospheric ducts were left out, as was the damping of radio waves due to the presence of rain and gas molecules. Also, only the linear sea model was considered (which is a good approximation for low to moderate winds only). Seas are also of nearly infinite depth, though the finite depth case is not much different. Finally, we make use of the Kirchhoff Approximation, which requires the high radius of curvature condition; this needs to be changed or adapted for HF radar.

The companion paper builds upon the theoretical elements exposed here and presents a closer analysis of the implementation of the simulation. It tackles in particular, the delicate question of the scene discretization, as well as the simulation of ship wakes, and gives an overview of the computational complexity associated to our approach. Finally, some simulated images in both monostatic and bistatic configurations are shown and analyzed.

References

[1] A. Arnold-Bos, A. Khenchaf, and A. Martin, "Bistatic radar imaging of the marine environment. Part II: simulation and results analysis," *IEEE Transactions on Geoscience and Remote Sensing, EUSAR '06 Special Issue*, 2007.

[2] G. Franceschetti, M. Migliaccio, D. Riccio, and G. Schirinzi, "SARAS: A Synthetic Aperture Radar (SAR) raw signal simulator," *IEEE Transactions on Geoscience and Remote Sensing*, vol. 30, no. 1, pp. 110–123, Jan. 1992.

[3] G. Franceschetti, M. Migliaccio, and D. Riccio, "On ocean SAR raw signal simulation," *IEEE Transactions on Geoscience and Remote Sensing*, vol. 36, no. 1, pp. 84–100, Jan. 1998.

[4] G. Franceschetti, A. Iodice, D. Riccio, G. Ruello, and R. Siviero, "SAR raw signal simulation of oil slicks in ocean environments," *IEEE Transactions on Geoscience and Remote Sensing*, vol. 40, no. 9, pp. 1935–1949, Sept. 2002.

[5] K. Oumansour, Y. Wang, and J. Saillard, "Multifrequency SAR observation of a ship wake," *Radar, Sonar and Navigation, IEE Proceedings*, vol. 143, no. 4, pp. 275–280, Aug. 1996.

[6] C. Cochin, T. Landeau, G. Delhommeau, and B. Alessandrini, "Simulator of ocean scenes observed by polarimetric SAR," in *Proceedings of the Comitee on Earth Observation Satellites SAR Workshop*, Toulouse, France, Oct. 1999.

[7] O. Airiau and A. Khenchaf, "A methodology for modeling and simulating target echoes with a moving polarimetric bistatic radar," *Radio Science*, vol. 35, no. 3, pp. 773–782, May-June 2000.

[8] L. A. Klein and C. T. Swift, "An improved model for the dielectric constant of sea water at microwave frequencies," *IEEE Transactions on Antennas and Propagation*, vol. AP-25, no. 1, pp. 104–111, 1977.

[9] J. V. Toporkov and G. S. Brown, "Numerical simulations of scattering from time-varying, randomly rough surfaces," *IEEE Transactions on Geoscience and Remote Sensing*, vol. 38, no. 4, July 2000.

[10] O. M. Philips, "The equilibrium range in the spectrum of wind-generated waves," *Journal of Fluid Mechanics*, no. 4, pp. 426–434, 1958.

[11] W. J. Pierson and L. Moskowitz, "A proposed spectral form of fully developped wind seas based on the similarity theory of S. A. Kitaigorodskii," *Journal of Geophysical Reasearch*, vol. 69, no. 64, pp. 5181–5190, 1964.

[12] A. K. Fung and K. K. Lee, "A semi-empirical sea-spectrum model for scattering coefficient estimation," *IEEE Journal of Oceanic Engineering*, vol. 7, no. 4, pp. 166–176, 1982.

[13] K. Hasselmann, T. P. Barnett, E. Bouws, H. Carlson, D. E. Cartwright, K. Enke, J. A. Ewing, H. Gienapp, D. E. Hasselmann, P. Kruseman, A. Meerburg, P. Müller, D. J. Olbers, K. Richter, W. Sell, and H. Walden, "Measurements of wind-wave growth and swell during the Joint North Sea Wave Project (JONSWAP)," *Deutsche Hydrographische Zeitung*, vol. 8, no. 12, pp. 1–95, 1973, suppl. A.

[14] T. Elfouhaily, B. Chapron, and K. Katarsos, "A unified directional spectrum for long and short wind-driven waves," *Journal of Geophysical Research*, vol. 102, no. C7, pp. 15 781–15 796, July 1997.

[15] M. S. Longuet-Higgins et al., *Ocean Wave Spectra*. Prentice-Hall, Inc., 1963, ch. Observations of the Directional Spectrum of Sea Waves Using the Motions of a Floating Buoy, pp. 111–136.

[16] M. Tucker and E. Pitt, *Waves in Ocean Engineering*, ser. Elsevier Ocean Engineering Book Series. Elsevier, 2001.

[17] C. Gelpi and K. Norris, "Estimated surface-wave contributions to radar Doppler velocity measurements of the ocean surface," *Remote Sensing of Environment*, vol. 87, pp. 99–110, 2003.

[18] R. Timman, A. J. Hermans, and G. C. Hsiaco, *Water waves and ship hydrodynamics*, ser. Mechanics of Fluids & Transport processes. Martins Njihoff Publishers & Delft University Press, 1985, no. ISBN 90-247-3218-2.

[19] W. Alpers, *Satellite Microwave Remote Sensing*. Chichester, U.K.: Ellis Horwood, 1983, ch. Imaging ocean surface waves by synthetic aperture radar – A review, pp. 107–119.

[20] R. Harger, *Wave Dynamics and Radio Probing of the Ocean Surface*. Plenum, 1986, ch. The SAR image of short gravity waves on a long gravity wave, pp. 371–392.

[21] M. Saillard, P. Forget, G. Soriano, M. Joelson, P. Broche, and P. Currier, "Sea surface probing with L-band Doppler radar : experiment and theory," *C. R. Physique*, vol. 6, no. 6, pp. 675–682, 2005.

[22] G. Soriano, C.-A. Guérin, and M. Saillard, "Scattering by two-dimensional rough surfaces: comparison between the method of moments, the kirchhoff and the small-slope approximation," *Waves in Random Media*, vol. 12, no. 1, Jan. 2002.

[23] G. Soriano and M. Saillard, "Modelization of the scattering of electromagnetic waves from the ocean surface," *Progress in Electromagnetics Research*, vol. X, chapter 4, pp. 102–128, 2003.

[24] G. R. Valenzuela, "Theories for the interactions of electromagnetic and oceanic waves – a review," *Boundary-Layer Meteorology*, vol. 13, no. 61-85, 1978.

[25] L. M. Brekjovskikh, "Difrakciya voln na neronoj poverhnosti: 1. obschaya teoriya," *Zh. Eksp. Teor. Fiz.*, vol. 23, pp. 275–288, 1952.

[26] ——, "Difrakciya voln na neronoj poverhnosti: 2. prilosheniya obschej teorii," *Zh. Eksp. Teor. Fiz.*, vol. 23, pp. 289–304, 1952.

[27] P. Beckmann and A. Spizzichino, *The Scattering of Electromagnetic Waves from Rough Surfaces*. New York, NY: Macmillan Co., 1963.

[28] F. T. Ulaby, R. K. Moore, and A. K. Fung, *Microwave Remote Sensing: Active and Passive, vol. II*. Artech House, 1986.

[29] D. E. Barrick, "Rough surface scattering based on the specular point theory," *IEEE Transactions*, vol. AP-16, pp. 449–454, 1968.

[30] C. Cox and W. Munk, "Statistics of the sea surface derived from sun glitter," *Journal of Marine Research*, vol. 13, pp. 198–227, 1954.

[31] S. O. Rice, "Reflection of electromagnetic waves from slightly rough surfaces," *Comm. Pure Appl. Math.*, no. 4, pp. 351–378, 1951.

[32] J. W. Wright, "Backscattering from capillary waves with application to sea clutter," *IEEE Transactions*, vol. AP-14, pp. 749–754, 1966.

[33] ——, "A new model for sea clutter," *IEEE Transactions*, vol. AP-16, pp. 217–223, 1968.

[34] A. Ishimaru, *Wave Propagation and Scattering In Random Media (Vol. 2)*. Academic Press, 1978.

[35] F. G. Bass and I. M. Fuks, *Wave Scattering from Statistically Rough Surfaces.* New York: Pergamon Press, 1979.

[36] H. Chan and A. K. Fung, "A theory of sea scatter at large incident angles," *Journal of Geophysical Research*, vol. 82, pp. 3439–3444, 1977.

[37] A. Khenchaf and O. Airiau, "Bistatic radar moving returns from sea surface," *IEICE Transactions on Electronics*, vol. E83-C, no. 12, Dec. 2000.

[38] A. Khenchaf, "Bistatic scattering and depolarization by randomly rough surfaces: application to the natural rough surfaces in X-band," *Waves in Random Media*, vol. 11, pp. 61–89, 2001.

[39] E. J. Walsh, M. L. Banner, J. H. Churnside, J. A. Straw, D. C. Vandemark, C. W. Wright, J. B. Jensen, and S. Lee, "Visual demonstration of three scales sea-surface roughness under light wind conditions," *IEEE Transactions on Geoscience and Remote Sensing*, vol. 43, no. 8, Aug. 2005.

[40] T. M. Elfouhaily and C.-A. Guérin, "A critical survey of approximate scattering wave theories from random rough surfaces," *Waves in Random Media*, vol. 14, no. 4, pp. R1–R40(1), Oct. 2004.

[41] A. G. Voronovich, "Small-slope approximation for electromagnetic wave scattering at a rough interface of two dielectric interfaces," *Waves in Random Media*, vol. 4, pp. 337–367, 1994.

[42] A. G. Voronovitch and V. U. Zavorotni, "Theoretical model for scattering of radar signals in Ku- and C-bands from a rough sea surface with breaking waves," *Waves in Random Media*, no. 11, pp. 247–269, 2001.

[43] A. Awada, M. Y. Ayari, A. Khenchaf, and A. Coatanhay, "Bistatic scattering from an anisotropic sea surface: Numerical comparison between the first-order SSA and the TSM models," *Waves in Random Media*, vol. 16, no. 3, Nov. 2006.

[44] G. Franceschetti, A. Iodice, D. Riccio, and G. Ruello, "Fractal surfaces and electromagnetic extended boundary conditions," *IEEE Transactions on Geoscience and Remote Sensing*, vol. 40, no. 5, pp. 1018–1031, May 2002.

[45] ——, "Extended boundary condition method for scattering and emission for natural surfaces modeled by fractals," *IEEE Transactions on Geoscience and Remote Sensing*, vol. 43, no. 5, pp. 115–1125, May 2005.

[46] L. Guo and Z. Wu, "Application of the extended boundary condition method to electromagnetic scattering from rough dielectric fractal sea surface," *Journal of Electromagnetic Waves and Applications*, vol. 18, no. 9, pp. 1219–1234, 2004.

[47] S. G. T. Elfouhaily and D. R. Thompson, "Formal tilt invariance of the local curvature approximation," *Waves in Random Media*, vol. 13, no. 4, p. L7, 2003.

[48] "APL-UW high-frequency ocean environmental acoustic models handbook," Advanced Physics Laboratory, University of Washington, Tech. Rep. TR 9407, Oct. 1994.

[49] R. K. Moore and A. K. Fung, "Radar determination of winds at sea," *Proceedings of the IEEE*, vol. 67, no. 11, Nov. 1979.

[50] M. W. Long, *Radar Reflectivity of Land and Sea*, 3rd ed. Artech House, 2001, no. ISBN 1-58053-153-9.

Andreas Arnold-Bos was born in 1981 in Schlieren (ZH), Switzerland. He received the aerospace engineering degree as well as the Research Master (II) in signal and image processing from SUPAERO, Toulouse, France in 2004. He has since then started a Ph.D. thesis –due by end 2007– at the E^3I^2 laboratory of the ENSIETA, an engineering school headed by the French Ministry of Defense. His past and current research interests involve optical computer vision, autonomous vehicles and radar signal exploitation.

Ali Khenchaf received his master degree of "Statistical Data Processing" from the University of Rennes I, in 1989. From 1989 till 1993, he was a researcher at IRCCyN (UMR CNRS 6597) Laboratory in Nantes, France. His researches and teaching courses are in the fields of numerical mathematics, electromagnetic wave propagation, waves and microwave, signal processing and operational research theory. In 1992, he received his Ph.D degree in Electronic Systems and Computer Network from the University of Nantes. From 1993 to 2001, he held an assistant professor position at the same university. Since September 2001, he joined ENSIETA, where he is now a Professor and the head of laboratory E^3I^2 (EA3876). His research interests include radar waves scattering, microwave remote sensing, electromagnetic wave propagation, scattering in random media, bistatic scattering of electromagnetic waves and target parameters estimation.

Arnaud Martin was born in Bastia, France in 1974. He received a PhD degree in Signal Processing (2001), and Master in Probability (1998) from the university of Rennes, France. Dr. Arnaud Martin worked on speech recognition during three years (1998-2001) at France Telecom R&D, Lannion, France. He worked in the department of statistic and data mining (STID) of the IUT of Vannes, France, as temporary assistant professor (ATER) during two years (2001-2003). In 2003, he joined the laboratory E^3I^2 (EA3876) at the ENSIETA, Brest, France, as a teacher and researcher. Dr. Arnaud Martin teaches mathematics, data fusion, data mining, signal processing and computer sciences. His research interests are mainly related to the belief functions for the classification of real data and include data fusion, data mining, signal processing especially for sonar and radar data.